Assessment of an extended Nijboer-Zernike approach for the computation of optical point spread functions

Joseph Braat
Optics Research Group, Department of Applied Sciences,
Delft University of Technology,
Lorentzweg 1, NL-2628 CJ Delft, The Netherlands
E-mail: j.j.m.braat@tnw.tudelft.nl

Peter Dirksen
Philips Research Laboratories, WAG-01
NL-5656 AA Eindhoven, The Netherlands
E-mail: peter.dirksen@philips.com

Augustus J.E.M. Janssen
Philips Research Laboratories, WY-81
NL-5656 AA Eindhoven, The Netherlands
E-mail: a.j.e.m.janssen@philips.com

Abstract

We assess the validity of an extended Nijboer-Zernike approach based on recently found, Bessel series representations of diffraction integrals comprising an arbitrary aberration and a defocus part, for the computation of optical point spread functions of circular, aberrated optical systems. These new series representations yield a flexible means to compute optical point spread functions, both accurately and efficiently, under defocus and aberration conditions that seem to cover almost all cases of practical interest. Because of the analytic nature of the formulas, there are no discretization effects limiting the accuracy as opposed to the more commonly used numerical packages based on strictly numerical integration methods. Instead, we have an easily managed criterion, expressed in the number of terms to be included in the Bessel series representations, guaranteeing desired accuracy. For this reason, the analytic method can also serve as a calibration tool for the numerically-based methods. The analysis is not limited to point-like objects but can also be used for extended objects under various illumination conditions. The calculation schemes are simple and permit to trace the relative strength of the various interfering complex amplitude terms which contribute to the final image intensity function.

OCIS codes: 000.3860, 000.4430, 050.1960, 070.2580, 110.2990, 110.3960

1 Introduction

In optical imaging, an exact knowledge of the optical impulse response or point spread function is required for the calculation of the image intensity pattern in the presence of more complicated objects. Analytical expressions for the point spread function are available in some simple cases if the wave-front exiting from the exit pupil is spherical and the transmission function of the optical system is uniform over a certain region (e.g. an annular pupil). In all other cases, numerical approaches based on integration of the complex amplitude over the exit pupil area are used.

An analytical expression for the impulse response in the aberration-free case for an out-of-focus position has been provided for the first time by Lommel (see Ref.[1], Sec. 8.8). The impulse response in the presence of (small) aberrations has been studied by Nijboer and Zernike who used orthogonal expansions involving Zernike polynomials to evaluate the impulse response. Their approach poses problems if the wave-front aberration function W approaches values in excess of $\lambda/4$, say 1 λ, because of the appearance of products of Zernike polynomials in the higher-order expansion terms; such products seemed rather untractable at that time. We remind the reader that the Nijboer-Zernike theory is an approximation for moderate values of the numerical aperture, not significantly larger than a value of 0.60 . Beyond this value, the quadratic approximation to the pathlength difference occurring in the exponential of the integrand of the diffraction integral is questionable. In Appendix A we present the higher order wave-front terms which are needed for a correct representation of defocusing in high-aperture systems. With this extension, the pathlength due to defocusing is correctly accounted for if the NA-value approaches 0.90 . However, beyond the value of 0.70, a more rigorous treatment involving the state of polarization of the focusing wave is needed [2]. The polarization-dependent effects become clearly visible at aperture values as large as 0.8 . In this paper, we will limit ourselves to the scalar diffraction integral although an extension to the vectorial case is possible along the lines of our analysis, the number of integrals to be evaluated being six (three for each orthogonal polarization state) instead of one.

The basic scalar diffraction integral to be evaluated for obtaining the spatial impulse response $U(x,y)$ in image space reads (see Ref.[1], Sec. 9.1)

$$\begin{aligned} U(x,y) &= \frac{1}{\pi} \iint_{\nu^2+\mu^2\leq 1} A(\nu,\mu) \exp\{i\Phi(\nu,\mu)\} \exp\left\{i(\nu^2+\mu^2)f\right\} \\ &\qquad \times \exp[i2\pi(\nu x+\mu y)] d\nu d\mu \\ &= \frac{1}{\pi} \int_0^1 \rho \exp(if\rho^2) \Big(\int_0^{2\pi} A(\rho,\theta) \exp\{i\Phi(\rho,\theta)\} \\ &\qquad \times \exp\{i2\pi r\rho\cos(\theta-\phi)\}\ d\theta \Big) d\rho \quad , \end{aligned} \tag{1}$$

where ν and μ are the normalized coordinates of a general point on the exit pupil sphere and (x,y) are the image plane coordinates (see Fig.(1)); with some liberal use of notation, we introduced the amplitude transmittance function $A(\rho,\theta)$ of the optical system and the wave-front aberration, $\Phi(\rho,\theta)$, expressed in radians. The transformation from cartesian to polar coordinates on the exit pupil sphere and in the image plane is formally written as $\nu+i\mu=\rho\exp(i\theta)$

and $x + iy = r\exp(i\phi)$.

The factor f represents the defocusing ($f = \pi/2$ corresponds to one focal depth). Within the framework of Zernike expansions, it is possible to treat the defocusing term and the aberrational term on an equal footing. However, from the physical point of view, the aberrational term is an intrinsic error of the optical system while the defocusing is a deliberately introduced defect which can take on values that are relatively large with respect to the aberrations of the system. For this reason, a separate treatment is commonly preferred and in this paper we largely adhere to this preference.

We refer to Ref.[3] and Ref.[1], Ch. 9, Secs. 9.1-4 and Appendix VII for an extensive exposition of the Nijboer-Zernike theory. As in Ref. [4], Sec. 1, we expand the point spread function U of Eq.(1) as

$$\begin{aligned} U(x,y) &= \frac{1}{\pi}\sum_{k=0}^{\infty}\frac{i^k}{k!}\int_0^1 \rho\exp(if\rho^2)\Big(\int_0^{2\pi}\Phi^k(\rho,\theta+\phi) \\ &\qquad \times \exp\{i2\pi r\rho\cos\theta\}\ d\theta\Big)d\rho \quad . \end{aligned} \tag{2}$$

Here, the amplitude transmission function $A(\rho,\theta)$ has been put equal to unity. Next the aberration function Φ is represented as

$$\Phi(\rho,\theta) = \sum_{n,m}\alpha_{nm}R_n^m(\rho)\cos m\theta\ , \tag{3}$$

where $R_n^m(\rho)$ are the Zernike polynomials. The expansion in Eq.(3) is in terms of orthogonal functions $R_n^m(\rho)\cos m\theta$ on the unit circle and contains only terms with integers $n, m \geq 0$ such that $n-m$ is even and ≥ 0. When aberrations are small, so that truncation of the infinite series in Eq.(2) after the term with $k = 1$ is allowed, we get (using elementary properties of Bessel functions) to a good approximation

$$\begin{aligned} U(x,y) &\approx 2\int_0^1 \rho\exp(if\rho^2)J_0(2\pi\rho r)d\rho\ + \\ &\qquad 2i\sum_{n,m} i^m\alpha_{nm}\int_0^1 \rho\exp(if\rho^2)R_n^m(\rho)J_m(2\pi\rho r)d\rho\cos m\phi. \end{aligned} \tag{4}$$

The reduction of the integrals in Eq.(4) is rather cumbersome. The method proposed by Nijboer, see Ref.[1], Sec. 9.4 and Ref.[3], is based on the expansion of $\exp(if\rho^2)$ as a series involving Zernike polynomials. The method requires an ad-hoc method for representing products of two Zernike polynomials as a finite linear combination of Zernike polynomials with a prescribed upper index m. Finally, the basic identity

$$\int_0^1 \rho R_n^m(\rho)J_m(2\pi\rho r)d\rho = (-1)^{\frac{n-m}{2}}\ \frac{J_{n+1}(2\pi r)}{2\pi r} \tag{5}$$

is applied. However, to the knowledge of the authors the method of representing products of Zernike polynomials, has remained mainly in a guess-and-try stage, and thus yields useful

results only for relatively small values of n and m. This problem becomes even more serious when first order considerations as in Eq.(4) no longer suffice so that products of more than two Zernike polynomials occur due to terms at the right-hand side of Eq.(2) with $k \geq 2$ that must be included. For these reasons, the Nijboer-Zernike theory is not satisfactory when aberrations and defocus values are considered that have values of order unity or larger.

A different approach, yielding valid results when the defocus parameter is large, consists of applying certain methods from asymptotic analysis. These methods are of limited use when one is interested in accurate computation of the point spread functions, especially when f is neither very small or very large. For the latter cases, it has become common practice to compute the integrals in Eq.(1) and/or Eq.(2) by using strictly numerical integration methods. In these numerical methods, one has inevitably to cope with the problem of selecting integration grids, preferably covering a square region in the (ν, μ)-plane so as to be able to take advantage of the computational efficiency of FFTs, to approximate integrals of functions that are inherently discontinuous (viz. at the edges of the pupil $\nu^2 + \mu^2 \leq 1$). In the frequently occurring cases that one uses a commercial software package for evaluating diffraction integrals (e.g. SOLID-C [5]), one has, furthermore, normally only limited access to the source codes and hence, a quality assessment of the obtained results is not feasible. Moreover, the result produced by these software packages is the image intensity distribution whereas a knowledge of the complex amplitude terms yields a more profound understanding of the final result.

In this paper we propose to use the analytic formulas of the Lommel type that were found in Ref.[4] for integrals as they occur in Eq.(4), and for similar integrals as in Eq.(4), with $R_n^m(\rho)$ replaced by the monomial ρ^n where $n - m \geq 0$ and even. As explained in Ref.[4], Sec. 3, any of the integrals involving Φ^k in Eq.(2) can be reduced to a finite sum of integrals of the type just mentioned, whence we have an analytic means to calculate $U(x, y)$. Alternatively, one can find it feasible to develop the complete complex pupil function $A \exp[i\Phi]$ in Eq.(1) in terms of Zernike polynomials and then we are in a similar position as in Eq.(4).

In this new approach, the through-focus calculation of the point spread function becomes feasible for much larger values of the wave-front aberration function than in the Nijboer-Zernike approach; both the defocus parameter and the aberration term may assume values comparable to or even larger than 2π in terms of the induced phase aberration without compromising the accuracy. Of course, the analysis extensively uses the properties of Zernike polynomials and supposes a circular geometry for the exit pupil. However, in principle, nonuniform amplitude distributions are permitted, and therefore, a noncircular pupil rim or a central obstruction could be accommodated, albeit at the expense of an increased number of higher order terms in the expansion. In the analysis presented in this paper, the azimuthal dependence of the Zernike polynomials is limited to a cosine- dependence. An extension to a general orientation of the wave-front aberration can easily be included. Even with this extension, the calculation scheme according to our analysis remains very short and its implementation into a symbolic program is easily realised.

This paper is organized as follows. In Section 2, the basic formulas are presented that are needed to treat the various practical examples in the subsequent sections. In Section 3, we present interpretations of our basic formulas in optical terms; this comprises an analogy of the formulas between the in-focus and defocused cases, symmetry properties of the image intensity distribution, and considerations about the radial extent of the impulse responses. In

Section 4, we consider computational aspects of our method, such as a verification of the convergence analysis developed in Appendix B and some basic problems concerning Zernike expansions as in Eq.(4). We also present in Section 4 a numerical comparison of our method with strictly numerical methods, such a those embodied by software packages. In Section 5, we study the imaging of an extended object for various coherence conditions; the impulse response approach clearly shows the separate origin of the background intensity terms and the coherence-based term of the intensity pattern. Finally, in Section 6 we apply our analysis to high-frequency aberration terms corresponding to a scattering-type of image blur. This type of unsharpness is present in multi-component optical systems with many glass-air transitions; it also plays a role in imaging through turbulent media, e.g. astronomical observation through the atmosphere. We will show that the impulse response approach to this type of blurred imaging is very robust and does not suffer from the numerical stability problems associated with the standard approach. Finally, in Appendix A, we analyse the defocusing term in the case of a high numerical aperture system and we present the expression for the coefficients of higher-order radial Zernike polynomials which have to be included in this case. In Appendix B, the maximum absolute value of the terms in the series expansion for the impulse response is given and a convergence criterion for the required number of terms in the series expansion is developed.

2 Basic formulas for the computation of $U(x, y)$

In this section we present the basic formulas to be used for the computation of U in the examples in the next sections. We start by expanding a general pupil function $A\exp(i\Phi)$ in terms of Zernike polynomials as

$$A(\rho,\theta)\exp[i\Phi(\rho,\theta)] = \sum_{n,m} \beta_{nm} R_n^m(\rho)\cos m\theta \tag{6}$$

with coefficients β_{nm} ($n \geq m \geq 0$, $n-m$ even) that are complex in general. The expansion in Eq.(6) of $A\exp(i\Phi)$ can be obtained, for instance, by a least squares fit of a finite series with sufficiently many terms to a (measured) pupil function $A\exp(i\Phi)$, a procedure which is common practice for expanding Φ itself. The efficient and reliable calculation of the coefficients β_{nm} for a general pupil function $A\exp(i\Phi)$ is still under study and will be treated in more detail in a forthcoming publication. It can be shown that the field U as defined by Eq.(4) is given by

$$U(x,y) = 2\sum_{n,m} \beta_{nm}\ i^m\ V_{nm}\cos m\phi \quad , \tag{7}$$

where

$$V_{nm} = \int_0^1 \rho\exp(if\rho^2)R_n^m(\rho)J_m(2\pi\rho r)d\rho \tag{8}$$

for integers $n, m \geq 0$ with $n-m \geq 0$ and even.

The Bessel series presentation for V_{nm} has been given in Ref.[4] and reads

$$V_{nm} = \exp(if)\sum_{l=1}^{\infty}(-2if)^{l-1}\sum_{j=0}^{p} v_{lj}\frac{J_{m+l+2j}(v)}{lv^l} \tag{9}$$

with v_{lj} given by

$$v_{lj} = (-1)^p (m+l+2j) \binom{m+j+l-1}{l-1} \binom{j+l-1}{l-1} \binom{l-1}{p-j} \Big/ \binom{q+l+j}{l} \quad , \qquad (10)$$

with $l = 1, 2, \ldots, j = 0, \ldots, p$. In (9) and 10 we have set

$$v = 2\pi r \quad , \qquad p = \frac{n-m}{2} \quad , \qquad q = \frac{n+m}{2} \quad . \qquad (11)$$

For the number L of terms to be included in the infinite series over l we have the following rule. When L=25, the absolute truncation error is of the order 10^{-6} for all f, v, n, m specified by

$$|f| \leq 2\pi, \quad v \leq 20, \quad 0 \leq p \leq q \leq 6 \quad . \qquad (12)$$

This is shown in Appendix B, in fact, the analysis given there can be easily adapted so as to yield a truncation criterion when different ranges than in (12) or different accuracy is required. Roughly one can say that one gets sufficient accuracy when the number L of included terms exceeds $3f$.

Returning to the commonly considered case where A in Eq.(6) equals unity and the aberration phase Φ is sufficiently small, one has the first order approximation

$$U(x,y) \approx 2V_{00} + 2i \sum_{n,m} \alpha_{nm}\, i^m\, V_{nm} \cos m\phi \quad , \qquad (13)$$

with α_{nm} now equal to the coefficients in the Zernike expansion of Φ, the aberration function in the pupil (see Eq.(8)).

To understand how the separate aberration terms $\alpha_{nm} R_n^m(\rho) \cos m\theta$ in the Zernike expansion of Φ contribute to the higher order terms $k = 2, 3, \ldots$ in the expansion of U in Eq.(2), it becomes awkward to use the V_{nm}-coefficients, as the result will involve products of Zernike polynomials that should be written as linear combinations with an appropriate upper index m. The approach used here (Ref.[4], Sec. 3) states that any term $k = 2, 3, \ldots$ in the series expansion of U in Eq.(2) is a linear combination of terms of the form

$$T_{nm} \cos m\phi \quad , \qquad (14)$$

with

$$T_{nm} = \int_0^1 \rho^{n+1} \exp(if\rho^2) J_m(2\pi\rho r) d\rho \qquad (15)$$

where n, m are non-negative integers such that $n - m \geq 0$ and even.

The Bessel series representation of T_{nm} closely resembles the expression for V_{nm} and is given in Ref.[4] as

$$T_{nm} = \exp(if) \sum_{l=1}^{\infty} (-2if)^{l-1} \sum_{j=0}^{p} t_{lj} \frac{J_{m+l+2j}(v)}{v^l} \qquad (16)$$

with the coefficients t_{lj} given by

$$t_{lj} = (-1)^j \ \frac{m+l+2j}{q+1} \ \binom{p}{j} \binom{m+j+l-1}{l-1} \Big/ \binom{q+l+j}{q+1} \quad , \qquad (17)$$

where $l = 1, 2, \ldots, j = 0, \ldots, p$. The truncation rule for the Bessel series representations of T_{nm} is the same as for the corresponding representations of V_{nm}, see Eq.(12).

For the case that a second or higher order approximation of U is required, one can establish formulas which, unfortunately, become rather complicated for increasing values of k. In certain special cases, such as

$$\Phi(\rho, \theta) = \alpha\rho^3 \cos\theta \ , \quad \gamma\rho^2 \cos 2\theta \ , \quad \delta\rho^4 \ , \tag{18}$$

that represent (uncorrected) coma, astigmatism and fourth order spherical aberration, respectively, a considerable short-cut of the general program is possible. In Ref.[4], Sec.4, such a thing is done for the first two cases in Eq.(18), and this yields expansions

$$U(x, y) = \sum_{j=0}^{\infty} C_j \ \alpha^j \quad , \qquad \sum_{j=0}^{\infty} D_j \ \gamma^j \quad , \tag{19}$$

with C_j, D_j expresssed explicitly in terms of the coefficients T_{nm} in Eq.(15). In Section 4 we shall use such an expansion for the third case (spherical aberration).

3 Physical interpretation of the basic formulas

In this section we show, starting from the aberration-free case, how the complex amplitude of an aberrated impulse response is built up from various interfering terms. We consider in this section the case that the aberration phase Φ has been expanded in a Zernike series as in Eq.(3), with $|\Phi|$ sufficiently small so that linearization as in Eq.(13) is allowed. The explicit form in Eq.(9) of the V_{nm} at the right-hand side of Eq.(7) shows a clear separation between the defocusing through powers f^{l-1} of f and the radial dependence through finite series involving Bessel functions $J_{m+l+2j}(v)$, evaluated at the argument $v = 2\pi r$. Finally, the azimuthal dependence in the series in Eq.(7) is represented by the factors $\cos m\phi$. Evidently, a separation of variables as we have here has advantages, both in terms of physical interpretation and from a computational point of view.

Before presenting our observations on the through-focus response of an aberrated optical system, we briefly recall the relationship between our normalized image plane coordinates (x, y) with defocus parameter f and the real space image coordinates (X, Y, Z) in the lateral and axial direction:

$$\begin{aligned} x &= X\frac{NA}{\lambda} \\ y &= Y\frac{NA}{\lambda} \\ v &= 2\pi\sqrt{x^2 + y^2} \\ f &= 2\frac{\pi}{\lambda}Z(1 - \sqrt{1 - NA^2}) \quad . \end{aligned} \tag{20}$$

In Appendix A, it is shown that, in case of systems with a high numerical aperture, the defocus term can be thought to be composed of a quadratic term and a term, represented by radial Zernike polynomials R_{2n}^0 with $n \geq 2$, that can be incorporated in the aberration phase.

3.1 Impulse response in focus ($f = 0$)

Referring to Eqs.(4) and (5), the aberration-free case with $f = 0$ leads to the well-known Airy function

$$U(x, y) = 2\frac{J_1(v)}{v} \quad . \tag{21}$$

The central spot is surrounded by a dark ring, corresponding to the first minimum of $J_1(v)$. The in-focus amplitude distribution in the presence of small aberrations was already given by Nijboer [3]: using the identity in Eq.(5) this yields for small aberrations

$$U(x, y) \approx 2\left(\frac{J_1(v)}{v} + \sum_{n,m} i^{m+1}\ \alpha_{nm}\ (-1)^{\frac{n-m}{2}}\ \frac{J_{n+1}(v)}{v}\cos m\phi\right) \quad . \tag{22}$$

3.2 Impulse reponse in the presence of defocus ($f \neq 0$)

In this subsection we concentrate on the physical interpretation of the quantities V_{nm} when $f \neq 0$ and the aberration is small.

The out-of-focus impulse response of a slightly aberrated optical system can be written per Eq.(13) as

$$U(x, y) \approx 2\left(V_{00} + \sum_{n,m}\ i^{m+1}\ \alpha_{nm}\ V_{nm}\cos m\phi\ \right) \quad , \tag{23}$$

where, as in the series in Eq.(22), the summation indices $n, m \geq 0$ and $n - m \geq 0$ and even. The quantities V_{nm} depend on f and v as shown in Eq.(9) with appropriate coefficients v_{lj} as given in Eq.(10). The close resemblance between Eqs.(22) and (23) stems from the representation of U in the defocused case in terms of the functions V_{nm} that substitute for the functions $(-1)^{\frac{n-m}{2}} J_{n+1}(v)/v$ in the in-focus situation. It is easily verified, see Eqs.(5, 9-10), that for $f = 0$, the functions V_{nm} reduce to the corresponding expressions comprising the Bessel functions of order $n + 1$.

The above formulas for $U(x, y)$ also lead to the symmetry properties for the intensity $I(x, y) = |U(x, y)|^2$ which were already enumerated in Ref.[1], Ch.9.4, and which we briefly recall for a single aberration term $\alpha_{nm} R_n^m(\rho)\cos m\phi$:

- The vertical axis is an m-fold symmetry axis; in particular, for $m = 0$ circular symmetry is present.
- When *m* is odd, the plane $z = 0$ is a symmetry plane.
- When m is even, the intensity at a position given by the cylindrical coordinates v, ϕ, z_0 is also found at the position $v, \phi + \pi/m, -z_0$.
- When $m = 0$, no symmetry with respect to the plane $z = 0$ is observed.
- When m is even and the aberration coefficient α_{nm} is replaced by $-\alpha_{nm}$, the intensity distribution remains the same when f is replaced by $-f$; in the case that m is odd and α_{nm} is replaced by $-\alpha_{nm}$, the intensities at ϕ and $\phi + \pi$ are the same.

We finally remark that the formulas also yield a good estimate of the radial extent of the impulse response once the maximum order of the radial Bessel function has been established. The first zero of the Bessel function of order n is found at a coordinate value given by $v \approx n+3$, and this yields an estimate of the lateral extent of the aberrated point spread function. For low argument values, the function $J_n(v)$ of order n is proportional to v^n. In this respect, it is interesting to note that in the presence of nonzero values of m, the expressions for V_{nm} (Eq.(9)) and T_{nm} (Eq.(16)) contain Bessel functions with a minimum index value of $m+1$. This value $m+1$ indicates that the contribution to the total amplitude of the point spread function is small for low v-values and that the spread (typically to a v-value of $m+4$) of the impulse response increases when the azimuthal index m of the coefficients α_{nm} or β_{nm} becomes larger.

In Fig.(2) we have presented the function V_{nm} for various combinations of n and m and, in each case, for a defocus parameter value 0 and π. Both the real and imaginary part of V_{nm} have been displayed, as well as its modulus squared $|V_{nm}|^2$ which corresponds to the image space intensity when only the single aberration term $R_n^m(\rho)\cos m\phi$ would be present.

4 Computational aspects and numerical comparison

In this section we restrict ourselves to the scalar diffraction integral with the resulting impulse response given by Eq.(1). We first give a number of computational considerations concerning the series representations in Eq.(9). As an example we consider the case that the aberration $A\exp(i\Phi)$ is given as

$$A \equiv 1 \quad , \qquad \Phi(\rho) = \alpha_{4,0} R_4^0(\rho) = \frac{2\pi}{6}(6\rho^4 - 6\rho^2 + 1) \ , \qquad 0 \le \rho \le 1 \ , \tag{24}$$

and we present specific convergence results for $V_{4,0}$. Next a comparison of our method with strictly numerical methods is made from a numerical point of view. Again we take Eq.(24) as an example. The coefficient $\alpha_{4,0}$ in (24) is chosen $2\pi/6$ since this corresponds to the 'just' diffraction-limited case in the best-focus position.

4.1 Computational aspects

We start by verifying the rule of thumb developed in Appendix B that the number L of terms that should be included in Eq.(9) for accuracy 10^{-4} should be of the order $3f$. In Table 1 we present the quantity

$$\max_{|v|\le 30} \left| |V_{4,0}(L)|^2 - |V_{4,0}(40)|^2 \right| \ , \tag{25}$$

with $f = 2\pi$ as a function of L. Here $V_{4,0}(L)$ is the right-hand side series in Eq.(9), truncated after L terms; we take $V_{4,0}(40)$ as reference.

As to the computation of the coefficients v_{lj} and the Bessel functions $J_n(v)$ that occur at the right-hand side of Eq.(9) we have the following comments. For low values of l and j we can use the binomial function 'choose k from n' since we have presented the v_{lj} as a combination of binomials. For the case that v_{lj} is needed for very large values of l and j (we have not seen

such large values in our simulations) we may note that, see Eq.(10),

$$B(l;a,b,c,d) := \binom{a+l-1}{l-1}\binom{b+l-1}{l-1}\binom{l-1}{c}\Big/\binom{d+l}{l} \tag{26}$$

satisfies the recursion

$$B(l+1;a,b,c,d) := \frac{(l+1)(l+a)(l+b)}{l(l-c)(l+d+1)}B(l;a,b,c,d) \quad . \tag{27}$$

For the computation of the Bessel function one can use the recursion formulas as given in Ref.[6], 9.1.27 on p. 361 (when these are not already present in the software environment of the user).

A further issue is the computation of the coefficients β_{nm} in the expansion

$$A(\rho,\theta)\exp[i\Phi(\rho,\theta)] = \sum_{n,m}\ \beta_{nm}R_n^m(\rho)\cos m\theta \ . \tag{28}$$

We are presently in the process of investigating methods to do this accurately and efficiently, see, for instance, Ref.[7].

Consider the example of spherical aberration in Eq.(24). We have an analytic expression for $U(x,y)$, in this case in terms of the T_{nm}'s of Eqs.(15-17); this expression follows in a similar fashion as the explicit expressions in Ref.[4], Sec. 4 for coma and astigmatism (also see Eqs.(18-19)). There holds

$$U(x,y) = 2\exp(i\alpha_{4,0})\sum_{k=0}^{\infty}\frac{(6i\alpha_{4,0})^k}{k!}T_{4k,0} \quad , \tag{29}$$

where the $T_{4k,0}$ are computed with defocus parameter $f-6\alpha_{4,0}$ instead of f. Using a simple least squares fit method where we included at the right-hand side of Eq.(28) all terms involving $R_{2n}^0(\rho)$ with $n \le N$, we found the following result. The maximum intensity deviation for values of f equal to -2π, 0 and $+2\pi$ according to

$$\max_{|v|\le 30}\left||U|^2-|U_N|^2\right| \quad , \tag{30}$$

where the index N refers to the number of included terms in Eq.(28), decreases to a level of 10^{-8} for N=6 (the maximum degree n is limited to 12). Hence we see a quite satisfactory 10^{-8} accuracy with a relatively modest number of terms at the right-hand side of Eq.(28).

4.2 Comparison with strictly numerical methods

In this subsection we present the results of a comparison of our method and two purely numerical methods to evaluate U. For this comparison we consider the example in Eq.(24), and we use the analytic formula in Eq.(29) or the U_N of Eq.(30) with N=6 (the latter U_N can be identified with the true U for the present purposes; see end of Subsection 4.1). A comparison purely in terms of CPU-time is not feasible at this moment since we are still investigating methods for the accurate and efficient determination of the β_{nm}. Therefore, we focus here on different aspects of such a comparison.

There are the following advantages of our method.

1. The representation of U as a series in Eq.(7) with the V_{nm}'s as given in Eqs.(8-10) yields a certain physical interpretation as well as computational advantages, see the beginning of Sec. 3.

2. The U obtained in our method is the complex amplitude of the response of the system when a true delta function has been presented as input. Software packages normally deliver intensities and use finite-extent 'delta'-functions.

3. Aside from the issue how many terms should be included in the series in Eq.(7), the computation of the terms themselves can be done with prescribed accuracy using the convergence analysis (the $3f$-rule) of Appendix B. The source codes of a (commercial) package are normally not readily available, whence a quality assessment is more difficult here.

4. Our codes are relatively simple

We have computed $I(x,y) = |U(x,y)|^2$ with the aberration term given by Eq.(24) and f=0 and $\pm 2\pi$ by using a typical integration procedure based on a set of grid points on a polar mesh in the pupil. With the number of grid points N_g equal to 10^4, the intensity values differed by 5.10^{-5} from the true ones, proving the limitation of the general-purpose strictly numerical method to an accuracy of the order of $1/N_g$. Fig.(3) illustrates this result by means of the dashed curve (analytic result, see Eq.(29)) and the curve with the open circles (strictly numerical method) which both apply to the true delta function response. The maximum difference of approximately 10^{-4} between both curves is not visible in the Figure.

A second comparison was made by using the software package SOLID-C [5], a frequently used simulation tool for optical imaging in lithography. As noted in 2) above, we have to consider an extended object, and for this we take a rectangular contact hole with side lengths of 300 nm in an opaque mask. Recalling our conventions as given by Eq.(20), we have chosen a wavelength λ=248 nm, NA=0.20, the aberration $A\exp(i\Phi)$ is the one of Eq.(24), and the defocus parameter equals f=-2π, 0, 2π. In our method we must convolve the complex impulse response U with the step function C that assumes the value 1 in the contact hole and 0 outside it. We have carried out this convolution by filling the contact hole with m^2 points (m=3,5,9,15,25 and 50). The effect of using 625 instead of 225 points was only noticeable at the 10^{-5} intensity level. In Fig.(3) we have displayed cross-sections of the intensity profiles $|U \otimes C|^2$ with C the step function describing the contact hole and $\otimes$ denoting convolution, and the intensity as obtained by the SOLID-C software package (all intensity levels have been normalized to unity, the on-axis value for the in-focus, aberration-free case). Inspection of the computed data shows that the deviations between the analytically based calculations and the SOLID-C results are of the order of 0.001 to 0.002; the curves in Fig.(3) show this difference (drawn curve for the analytically based computation and open squares for the SOLID-C results). The deviation of the SOLID-C results is most pronounced at low v-values.

5 Image formation by an extended object

In the case of image formation by an extended object, the illumination mode of the object plays an important role. For the general case of an object $F(x_0, y_0)$, illuminated in a partially coherent way, the intensity distribution in the image plane is given by:

$$I(x,y) = \iiiint \mu(x_0 - x_0', y_0 - y_0') F(x_0, y_0) F^*(x_0', y_0') \quad \times$$
$$U(x - x_0, y - y_0) U^*(x - x_0', y - y_0') dx_0 dx_0' dy_0 dy_0' \quad , \tag{31}$$

where $U(x, y)$ is the impulse response given by e.g. Eq.(23) and $\mu(x_0, y_0)$ is the mutual coherence function (see Ref.[1], Sec. 10.5.3.). This function is derived from the source intensity function with the aid of the Zernike-van Cittert theorem according to

$$\mu(x_0, y_0) = \frac{\iint I(p,q) e^{i(p(x_0) + iq(y_0))} dpdq}{\iint I(p,q) dpdq} \quad , \tag{32}$$

with $I(p, q)$ the intensity distibution of the source, observed on the exit pupil sphere of the imaging system; (x_0, y_0) are general normalized coordinates in the image plane.

In the case of a standard illumination function with circular symmetry, the coherence factor σ is commonly used which gives the ratio between the source radius and the exit pupil radius. In this case, the mutual coherence function is given by the circularly symmetric function

$$\mu(v) = \frac{2J_1(\sigma v)}{\sigma v} \quad . \tag{33}$$

We note that other commonly used illumination modes such as quadrupole, annular or decentered source configurations lead to comparable analytical mutual coherence functions $\mu(x_0, y_0)$.

We will now analyze some situations which are frequently encountered in optical lithography, ranging from coherently illuminated objects to the case of full incoherence in the illumination. Note that in our analysis the value of σ is not limited to unity but can be extended to values ≥ 1.

5.1 Coherent imaging

In high-resolution optical lithography, one often enhances the imaged features by manipulating phase structures on the mask. In the case of a fairly coherent imaging process ($\sigma \ll 1$), phase shifting features on the mask are most effective; the fully coherent case with $\sigma = 0$ then is a fair approximation (the source is a delta function $I(p, q) = \delta(p, q)$. The corresponding mutual coherence function $\mu(x_0, y_0)$ equals unity and the image plane intensity is given by

$$I(x,y) = |F(x_0, y_0) \otimes U(x_0, y_0)|^2 \quad . \tag{34}$$

5.2 Incoherent imaging

In optical lithography, the imaging of a so-called binary mask requires a value of $\sigma \sim 1$ and the imaging process can be approximated by the fully incoherent case $\sigma = \infty$ where the source intensity equals unity up to infinity. The mutual coherence function now becomes a delta function: $\mu(x_0, y_0) = \delta(x_0, y_0)$ and the image intensity distribution is given by

$$I(x, y) = |F(x_0, y_0)|^2 \otimes |U(x_0, y_0)|^2 \quad . \tag{35}$$

This results in an optical system that is now linear in intensity.

5.3 Partially coherent imaging

We now simulate the lithographic imaging process by means of a sequence of spatial delta-functions that have imaging properties similar to contact holes. The exact shape of small contact holes is not very important, it is the area that determines their relative weight in the imaging process. Therefore, we approximate an array of contact holes by an array of delta functions, each having a complex amplitude:

$$F(x_0, y_0) = \sum_n A_n \delta(x_0 - a_n, y_0 - b_n) \quad . \tag{36}$$

Using Eq.(31), we obtain the image space intensity distribution

$$I(x, y) = \sum_{n,m} A_n A_m^* \, \mu(a_n - a_m, b_n - b_m) U(x - a_n, y - b_n) U^*(x - a_n, y - b_n) \; . \tag{37}$$

Here, the image formation is essentially a nonlinear process and it can not be written in terms of a convolution.

In Fig.(4) we present the results of applying Eq.(37) to the configuration of two closely spaced contact holes with a separation of 0.2 μm in an opaque mask. The aerial image intensity is depicted according to the analytic approach. One contact hole is considered to introduce a phase shift of π. For this reason, the intensity exactly midway the two holes is zero in the coherent case. As the coherence of the imaging is decreased (σ increases), the interference term weighted by $\mu(2a, 0)$ gradually vanishes and the individual intensity profiles corresponding to each object merge. In the Figure, we have also depicted the intensity profiles produced by the software package SOLID-C which here used finite size contact holes as the input pattern (circular holes with a diameter of 100 nm). From Fig.(4), one concludes that the approximation of the contact holes by means of a mathematical delta function is fully justified here; in each figure the deviations between the analytical and the SOLID-C curves do not exceed the typical value of 0.01 . The advantage of the analytical approach is the clear relationship between the interfering terms which generate the final image intensity pattern. During the design process of e.g. phase- and amplitude-assisted masks, a valuable insight is obtained in the relationship between the modulation depth and steepness of the image intensity pattern and the parameter choices for the mask transmission function. The extension to larger arrays of contact holes and the inclusion of defocus and aberrations is straightforward. In each case, starting with the fully coherent case, the interference effects can be studied using the analytic expression for the complex amplitude. The behavior in the partially coherent case is then obtained as an intermediate situation between the fully coherent and the incoherent case.

6 The impulse response in the presence of high-frequency aberration terms

In this section we present a computational result which is related to a high-frequency wave-front perturbation. It frequently occurs in practice that the wave-front aberration can not be adequately described by the standard series of low-frequency Zernike polynomials [8]. These Zernike polynomials are capable of describing the wave-fronts emerging from an optical system towards the axial and off-axis field points. Alternatively, if an optical system suffers from a lack of rotational symmetry due to minute tilting and centring errors of the constitutive elements, the wave-front converging to an image point on axis shows small basic residual aberration terms which can also be easily represented by means of lower order Zernike coefficients. On the other hand, manufacturing imperfections of the optical surfaces, spherical or aspherical, may turn up in the wave-front emerging from the optical system as higher-frequency components in the wave-front expansion which are outside the scope of the standard series of Zernike polynomials [9]. These high-frequency wave-front perturbations also constitute a serious problem in the frequently used numerical approach for the calculation of the diffraction image that is based on the Fast Fourier Transform method (FFT). Quickly varying patterns in the pupil function of the optical system complicate the sampling of the pupil function. Moreover, the extent of the diffraction image in the image plane is enlarged by the high-frequency content in the pupil function and this requires many more sampling points in the image plane. In practice, the number of required sampling points in pupil and image plane may exceed practical values like 2^{10} or, ultimately, 2^{12} in one dimension.

When using our approach based on the expansion of the complex pupil function in terms of Zernike polynomials, we exploit the simple relationship of Eq.(5) to translate the presence of a Zernike polynomial of radial order n into an image plane amplitude distribution given by a function of the type $J_{n+1}(v)/v$ (no defocusing). In the defocused case, the functions V_{nm} from Eq.(23) are needed.

In Fig.(5) we present a calculated intensity pattern in the presence of a set of high-frequency Zernike coefficients up to order n=25 which, in total, produce an *rms* wave-front aberration of $1/(2\pi)$=0.159 λ. The low-intensity part of the calculated pattern outside the central lobe resembles a speckle pattern; this can be explained by the uncorrelated nature of the high order Zernike coefficients α_{nm} of each polynomial contribution $\alpha_{nm} Z_n^m(\rho,\theta) = \alpha_{nm} R_n^m(\rho)\cos(m\theta)$.

7 Conclusion

We have implemented our extended Nijboer-Zernike analysis for the calculation of the diffraction point spread function in the case of both small and large aberration values. Throughout the analysis, the defocusing effect is taken as an independent parameter that can be incremented to several focal depths without any convergence problems. The number of required terms in the series expansion for the complex amplitude in the image space can be estimated by means of some simple expressions which comprise the value of the aberration terms or the defocusing parameter. In practice, the typical number L of terms needed amounts to 25, yielding an ac-

curacy of 10^{-5} in the image plane intensity while an extension of L to 40 brings us below the 10^{-10} value. Various comparisons with numerically based integration schemes have been carried out showing that an accuracy in intensity in the region of 10^{-5} to 10^{-3} is typical for these methods. This demonstrates that our analytical approach also has the capability of serving as a reference for these numerical methods.

The application of the analysis to the impulse response of an optical system leads to effective calculation schemes where one can fully exploit the separation of radial and azimuthal dependence in the expressions. We can easily extend our analysis to the case where the wavefront aberration is accompanied by a nonuniform amplitude distribution in the exit pupil of the optical system. An extension to the vectorial treatment of diffraction phenomena at high values of the numerical aperture has not been carried out so far, but the basic approach can equally be applied in this case, the main difference being the number of diffraction integrals to be evaluated (six instead of one).

We have studied not only the image of a point object, but also the imaging of extended object which are illuminated in a general, partially coherent manner. The analytical expressions permit a separate inspection of the various terms contributing to the complex image amplitude. This possibility can be exploited for the effective design of more complicated object structures, e.g. phase- and amplitude-shifting masks in optical microlithography. Moreover, we think that our method presents a serious advantage when dealing with high-frequency aberration terms. The sampling problem in pupil and image plane encountered in e.g. the FFT-approach is absent when using our analytic expressions.

Acknowledgement

The authors would like to thank the reviewers of this paper for their comments and recommendations which had a beneficial effect on the presentation of the subject of this paper.

Appendix A: The defocusing term as a function of numerical aperture

In Fig.(6) a spherical wave-front through P converges towards the real image point M_2. The defocused image is captured in a plane through M_1 and the axial defocus distance is z. The wave-front deviation W_f as a function of defocus is given by the optical distance PQ. To calculate this distance, we apply the cosine rule in triangle PM_1M_2

$$(W_f + R_1)^2 + z^2 + 2(W_f + R_1)z\cos p = R_2^2 \quad . \tag{A.1}$$

Using the property that, for all realistic situations, the wave-front deviation W_f is much smaller than R_1, we obtain

$$W_f = z\,[1 - \cos p] = z\left[1 - \sqrt{1 - \sin^2 p}\right] \quad . \tag{A.2}$$

The normalized coordinate on the exit pupil sphere through O and P is given by the ratio of the sine of a general ray and the sine of the marginal ray, $\rho = (\sin p)/s_0$ where $s_0 = \sin p_0 = NA$, and the wave-front deviation W_f now becomes

$$\begin{aligned} W_f &= z\left(\frac{\sin^2 p}{2} + \frac{\sin^4 p}{8} + \frac{\sin^6 p}{16} + \quad ...\right) \\ &= \frac{1}{2}zs_0^2\rho^2 \;+\; \frac{1}{8}zs_0^4\rho^4 \;+\; \frac{1}{16}zs_0^6\rho^6 \;+\; \cdots \quad . \end{aligned} \tag{A.3}$$

The complete phase term for defocus is obtained by multiplying W_f with the wave number $k = 2\pi/\lambda$.

Eq.(A.3) shows that for larger values of the numerical aperure $NA = s_0$ at the image side, the defocusing term resulting from the wave-front deviation W_f is not well approximated by $\frac{1}{2}kzs_0^2\rho^2$. A considerable enhancement is obtained by replacing $1 - \sqrt{1 - \sin^2 p}$ in Eq.(A.2) by its least squares quadratic approximation $\hat{b}_0 + \hat{b}_1\rho^2$. This then leads to the optimal second order approximation

$$W_f \approx \; z\left(\hat{b}_0 + \hat{b}_1\rho^2\right) \tag{A.4}$$

and a corresponding approximation $kz\left(\hat{b}_0 + \hat{b}_1\rho^2\right)$ for the defocusing term. It thus turns out that we obtain average approximation errors having at s_0=0.82 the same value as what we would obtain for s_0=0.60 when we approximate $1 - \sqrt{1 - \sin^2 p}$ by $\frac{1}{2}s_0^2\rho^2$.

A further extension of this methodology, allowing even higher values of s_0, is to develop the remaining approximation error $1 - \sqrt{1 - \sin^2 p} - \hat{b}_0 - \hat{b}_1\rho^2$ in a series involving the radial Zernike polynomials $R_{2n}^0(\rho)$ with $n = 2, 3, \cdots$ and to incorporate this error in the aberration phase Φ. One has in fact, with $\rho = (\sin p)/s_0$ as above,

$$\sqrt{1 - \sin p^2} = -\frac{1}{2}(1 - c_0)\sum_{n=0}^{\infty}\left[\frac{1}{2n-1}\left(\frac{1-c_0}{1+c_0}\right)^{n-1} - \frac{1}{2n+3}\left(\frac{1-c_0}{1+c_0}\right)^{n+1}\right] R_{2n}^0(\rho) \quad , \tag{A.5}$$

where $c_0 = \cos p_0$. The terms with $n = 3, 4, \cdots$ in the right-hand side are sufficiently small for values of the numerical aperture s_0 as large as 0.90 that they can be considered as small aberrations ($|f|$ as large as 2π).

Although the correct representation of the defocus term at high values of NA is important, it is not a sufficient extension to correctly describe the impulse response in this regime. The radiometric effects within the high numerical aperture beam have to be taken into account. By adopting a complex-valued parameter f, these radiometric amplitude variations on the pupil sphere can be accommodated. Of course, in a final step, the vectorial treatment of wave propagation as described in Ref.[2] has to be used.

Appendix B: Analysis of V_{nm} and T_{nm}

B.1. Bounds on V_{nm} and T_{nm}

There holds for all f, v and all allowed n, m

$$|V_{nm}| \leq \frac{M_m(v)}{2\sqrt{n+1}} \quad , \qquad |T_{nm}| \leq \frac{M_m(v)}{2n+2} \quad , \tag{B.1}$$

where

$$M_m(v) = \max_{0 \leq u \leq v} |J_m(u)| \leq 1 \quad . \tag{B.2}$$

The bounds in (B.1) follow easily from the integral representations in Eqs.(8),(15), where for the first bound we also use that

$$\int_0^1 \rho \, |R_n^m(\rho)|^2 \, d\rho = \frac{1}{2(n+1)} \quad , \tag{B.3}$$

together with the Cauchy-Schwarz inequality.

B.2. Truncation of infinite series.

We consider the series representations (9) and (16) of V_{nm} and T_{nm} for the range of f, v, n, m (p, q) indicated in Eq.(12). The main result is as follows. In the relevant range it is sufficient to include the first 25 terms of the infinite series over l to guarantee absolute accuracy of order 10^{-6}. Moreover, the truncation errors are in all cases of the same order of magnitude or smaller than the truncation error for the series

$$V_{00} = T_{00} = \exp(if) \sum_{l=1}^{\infty} (-2if)^{l-1} \frac{J_l(v)}{v^l} \quad . \tag{B.4}$$

Let us first consider the convergence behavior of the series in Eq.(B.4). It follows from the basic properties of the Bessel functions, such as 9.1.30 in Ref.[6], that $v^{-l} J_l(v)$ is positive and decreasing in $v \in [0, 20]$ when $l \geq$20. Hence the series in Eq.(B.4) exhibits worst case convergence behavior at $v =$0 where we have

$$\left. \frac{J_l(v)}{v^l} \right|_{v=0} = \frac{2^{-l}}{l!} \quad , \tag{B.5}$$

so that

$$V_{00}(v=0) = \frac{1}{2}\ \exp(if) \sum_{l=1}^{\infty} \frac{(-if)^{l-1}}{l!} \quad . \tag{B.6}$$

The convergence analysis of the series in Eq.(B.6) can be given by using Stirling's formula for $l!$. Thus the terms $(-if)^{l-1}/l!$ have modulus of order less than unity from $l = \lfloor ef \rfloor$ onwards. For f=2π we have $\lfloor ef \rfloor$=17, and $(2\pi)^{l-1}/l!$ decreases from 6.10^{-4} at $l = 20$ to 9.10^{-7} at $l = 25$. As a rule of thumb we get that the number L of terms to be included should be somewhat larger than ef; normally $L \geq 3f$ suffices.

We next compare the convergence behavior for the general cases V_{nm}, T_{nm} to the standard series V_{00}, T_{00}. Here it is enough to restrict attention to V_{nm}. This is possible since one gets from Eq.(10) and Eq.(17) that

$$\left| \frac{l^{-1} v_{lj}}{t_{lj}} \right| \ = \ \frac{(l-1)!}{q!\ p!} \ \frac{(q+j)!}{(l-1-p+j)!} \ , \quad j = 0, \ldots, p \ , \tag{B.7}$$

and the right-hand side of Eq.(B.7) $\geq$1 for all l, p, q that satisfy $l - 1 - p \geq q$. We shall thus consider the quantity, see Eq.(9) and Eq.(B.4)

$$Q_{lj} \ = \ \left| \frac{l^{-1}\ v_{lj}\ J_{l+m+2j}(v)}{J_l(v)} \right| \ , \quad j = 0, \ldots, p \ , \tag{B.8}$$

and our aim is to bound $\sum_{j=0}^{p} Q_{lj}$.

Noting that l is large compared to m, j, q we have from Eq.(10) and the definitions of p and q that

$$\begin{aligned} \left| l^{-1} v_{lj} \right| \ &\approx \ \frac{(l+m+j)!(l-1+j)!}{(l+q+j)!(l-1+j-p)!} \binom{p}{j} \binom{q+j}{p} \\ &\approx \ \exp\left(-(q+1)p/l\right)\ \binom{p}{j} \binom{q+j}{p} \quad . \end{aligned} \tag{B.9}$$

Furthermore there is the inequality

$$0 \leq \frac{J_s(v)}{J_{s-1}(v)} \leq \frac{v/s}{1+\sqrt{1-(v/s)^2}} \quad , \ \ 0 \leq v \leq s \ \ . \tag{B.10}$$

The latter inequality follows from Ref.[6], second formula in 9.1.73, for the continued fraction expansion of $J_s(v)/J_{s-1}(v)$, combined with the continued fraction expansion

$$\frac{1}{2} - \sqrt{\frac{1}{4} - c} \ = \ \frac{c}{1-}\ \frac{c}{1-}\ \frac{c}{1-} \quad \cdots \quad , \ 0 \leq c \leq \frac{1}{4} \ . \tag{B.11}$$

Applying (B.10) repeatedly we thus get that

$$0 \leq \frac{J_{l+m+2j}(v)}{J_l(v)} \leq b^{m+2j} \quad , \ \ 0 \leq v \leq l \ , \tag{B.12}$$

where

$$b \;=\; \frac{v/(l+1)}{1+\sqrt{1-(v/(l+1))^2}} \quad . \tag{B.13}$$

Combining (B.9) and (B.12) and using $m = q - p$ we get

$$\sum_{j=0}^{p} Q_{lj} \;\leq\; \exp\left(-(q+1)p/l\right) \sum_{j=0}^{p} \binom{p}{j}\binom{q+j}{p} b^{q-p+2j} \quad . \tag{B.14}$$

The maximum over $p = 0, \ldots, q$ of the series at the right-hand side of (B.14) occurs at $p = q$. A numerical inspection of the quantity

$$\exp\left(-(q+1)q/l\right) \sum_{j=0}^{q} \binom{q}{j}\binom{q+j}{q} b^{2j} \quad . \tag{B.15}$$

for the worst case l=24, v=20 (so that b=1/2) and $p = q = 0, 1, \ldots, 6$, yields a bound of the order 10 for the left-hand side of Eq.(B.14). This is sufficient for our purposes.

We have observed numerically that the absolute convergence behavior of the series for V_{nm} is actually better than what one might expect from the foregoing analysis. The reason for this is that some of the estimates (in particular (B.12)) are crude while the various worst cases do not occur simultaneously.

We may note that the truncation analysis can be extended to the cases of different ranges for the various parameters and variables. This is based on the observation that

$$\sum_{j=0}^{q} \binom{q}{j}\binom{q+j}{q} b^{2j} = P_q(1+2b^2) \approx \frac{\left(b+\sqrt{1+b^2}\right)^{2q+1}}{2(\pi b q)^{\frac{1}{2}}(1+b^2)^{\frac{1}{4}}} \quad , \tag{B.16}$$

where P_q is the Legendre polynomial of degree q, with asymptotic behavior as given in Ref.[10], Thm. 8.2.1. Accordingly one finds that for large l the worst case quantity in Eq.(B.15) behaves like $\exp\{-(q+1/2)(q+1/2-v)/l\}$.

For more information on the content of this paper, please contact:

Joseph Braat

Postal address:

Optics Research Group, Department of Applied Sciences,
Delft University of Technology,
Lorentzweg 1, NL-2628 CJ Delft, The Netherlands
E-mail: j.j.m.braat@tnw.tudelft.nl

or

Philips Research Laboratories WY3
Professor Holstlaan 4, NL - 5656 AA Eindhoven, The Netherlands
E-mail: joseph.braat@philips.com

References

[1] M. Born and E. Wolf, *Principles of Optics* (4th rev. ed., Pergamon Press, New York, 1970).

[2] B. Richards and E. Wolf, "Electromagnetic diffraction in optical systems II. Structure of the image field in an aplanatic system", Proc. Roy. Soc. London, A, **253**, 358-379 (1959).

[3] B.R.A. Nijboer, *The Diffraction Theory of Aberrations* (Ph.D. Thesis, University of Groningen, Groningen, 1942).

[4] A.J.E.M. Janssen, "An extended Nijboer-Zernike approach for the computation of optical point spread functions", to appear in J. Opt. Soc. Am.

[5] SOLID-C, a software product (release 5.6.2) from SIGMA-C GmbH, Thomas-Dehlerstrasze 9, D-81737 Munich (Germany)

[6] M. Abramowitz and I.A. Stegun, *Handbook of Mathematical Functions* (9^{th} printing, Dover Publications, New York, 1970).

[7] J.Y. Wang and D.E. Silva, "Wave-front interpretation with Zernike polynomials", Appl. Opt. **19**, 1510-1518 (1980).

[8] V.N. Mahajan, "Zernike circle polynomials and optical aberrations of systems with circular pupils", Appl. Opt. **33**, 8121-8124 (1994).

[9] C.J. Progler and A.K. Wong, "Zernike coefficients, are they really enough ?" in *Optical Microlithography XIII*, Ed. C.J. Progler, Proc. SPIE **4000**, 40-52 (2000).

[10] G. Szegö, *Orthogonal Polynomials* (4^{th} edition, American Mathematical Society, Providence, 1975).

Table Caption

Table 1

The convergence of the analytically calculated image intensity $I(x,y) = |U(x,y)|^2$ as a function of the number of terms L included in the series expansion for the amplitude U (interval $|v| \leq$30).

Figure Captions

Figure 1

Geometry of the wave propagating from the exit pupil (center at E_0) towards the image plane (center at P_0). The diameter of the exit pupil is $2\rho_0$ and the distance from pupil to image plane is R. The real-space image plane coordinates are (X,Y). In this paper, the exit pupil coordinates are normalised to unity by means of the value of ρ_0 and denoted by (ν,μ); the image plane coordinates are normalized with the aid of the diffraction unit, λ/NA, and denoted by (x,y). $NA(=\rho_0/R)$ is the image-side numerical aperture of the optical system.

Figure 2

The real part (left-hand column), imaginary part (central column) and the squared modulus or intensity (right-hand column) of various radial functions V_{nm} have been displayed, each time for two values of the defocus parameter f (drawn curve: $f = 0$, dashed curve: $f = \pi$). From top to bottom, the values of the indices (n,m) are, respectively, $(0,0)$, $(2,2)$, $(3,1)$ and $(4,0)$.

Figure 3

Cross-sections of the image intensity for a delta function object (labels 'Extended Nijboer-Zernike' and 'numerical integration') and for a rectangular contact hole in the object plane ('Extended Nijboer-Zernike, 0.3 μm hole' and 'SOLID-C, 0.3 μm hole). The aberration term is fourth-order spherical aberration and the magnitude is given by the value of $\alpha_{4,0}$ $(2\pi/6)$, corresponding to the 'just' diffraction-limited case. The deviations between the analytical computation and the strictly numerical integration method (typically 5.10^{-5}) are not visible in the figure; the deviations between the data obtained for the contact hole (typically 0.001 to 0.002) are especially visible for low values of the radial coordinate v.

Figure 4

Aerial image intensity calculation due to a mask with two contact holes (diameter 0.1 μm, spacing 0.2 μm). Solid lines: calculated using Eqs.(9)-(10) for the functions V_{nm}; Dashed lines: SOLID-C package, λ=0.248 μm, NA=0.6, in-focus situation. The typical difference in

normalized intensity between the two resulting curves amounts to 0.01 .

Figure 5

The image plane intensity distribution in the case of a set of high-frequency Zernike coefficients that represent the result of e.g. manufacturing errors in the wave-front exiting from an optical system. A set of coefficients in the range q=6,...,12 has been introduced (n ranges from 6 to 24, m from 0 to 12). The central maximum has been truncated in the plot. Note that the diffracted intensity is concentrated within a circle given by $v = n + 3$, the extent of the highest order Bessel function present in the image plane intensity function. The numerals representing the intensity in the contour plot are a measure for the relative intensity and have to be multiplied by 10^{-2}.

Figure 6

The wave-front deviation PQ in the case of defocusing. The spherical wave (radius R_2, center of curvature M_2) is projected on a defocused image plane through M_1 and perpendicular to the axis OM_2. The aperture angle is denoted by p. The defocus distance z has been heavily exaggerated in the figure.

Convergence of analytical calculation	
L	Maximum intensity difference
10	5.0×10^{0}
15	1.5×10^{-2}
20	8.4×10^{-5}
25	7.2×10^{-8}
30	5.1×10^{-11}
35	7.7×10^{-15}

Table 1:

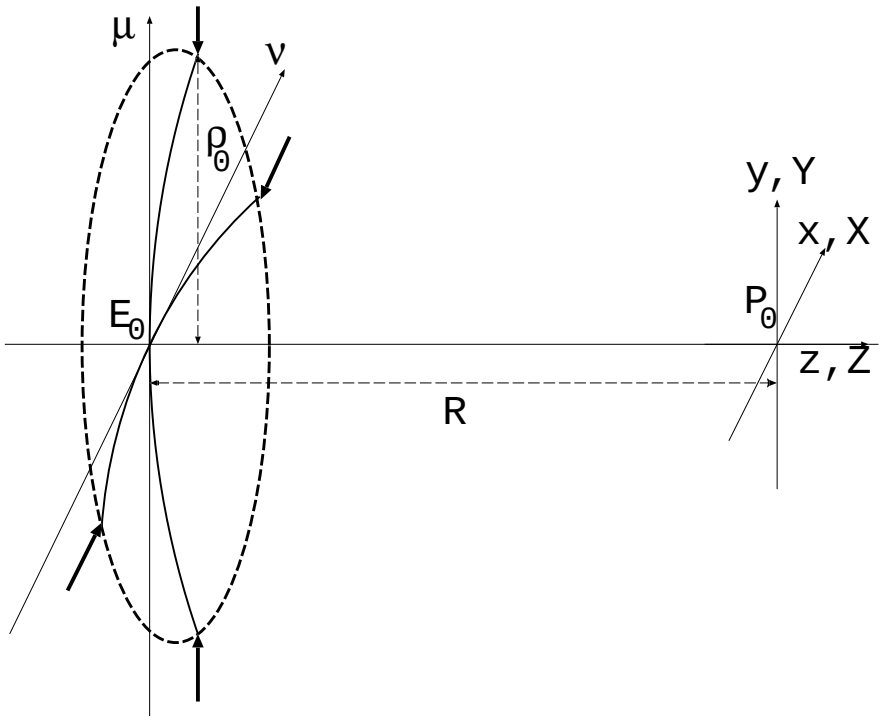

Figure 1:

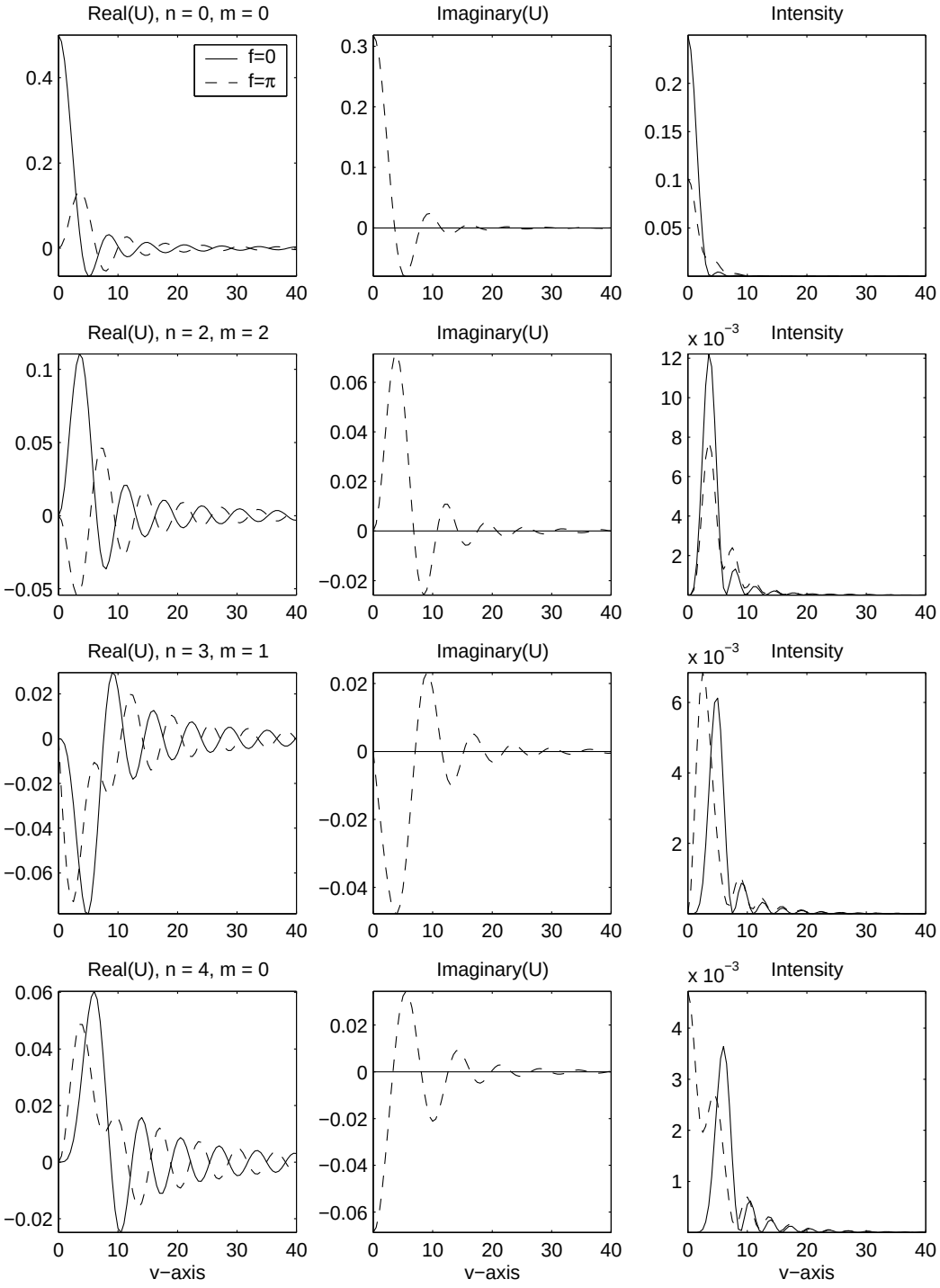
Real(U), n = 0, m = 0
f=0
f=π
Imaginary(U)
Intensity
Real(U), n = 2, m = 2
Imaginary(U)
x 10^−3
Intensity
Real(U), n = 3, m = 1
Imaginary(U)
x 10^−3
Intensity
Real(U), n = 4, m = 0
Imaginary(U)
x 10^−3
Intensity
v−axis
v−axis
v−axis

Figure 2:

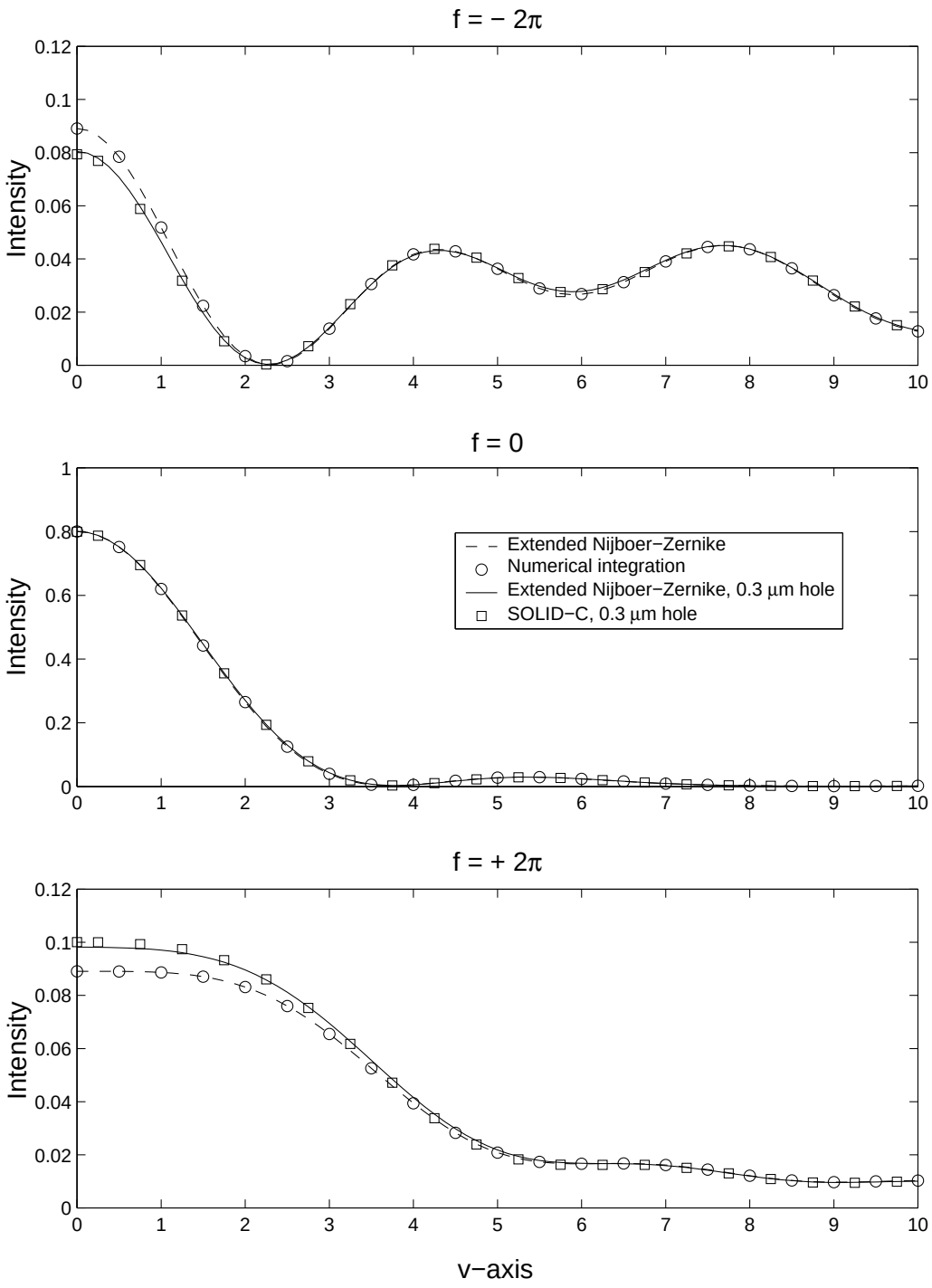
f = − 2π
f = 0
f = + 2π
Intensity
v−axis
Extended Nijboer−Zernike
Numerical integration
Extended Nijboer−Zernike, 0.3 μm hole
SOLID−C, 0.3 μm hole

Figure 3:

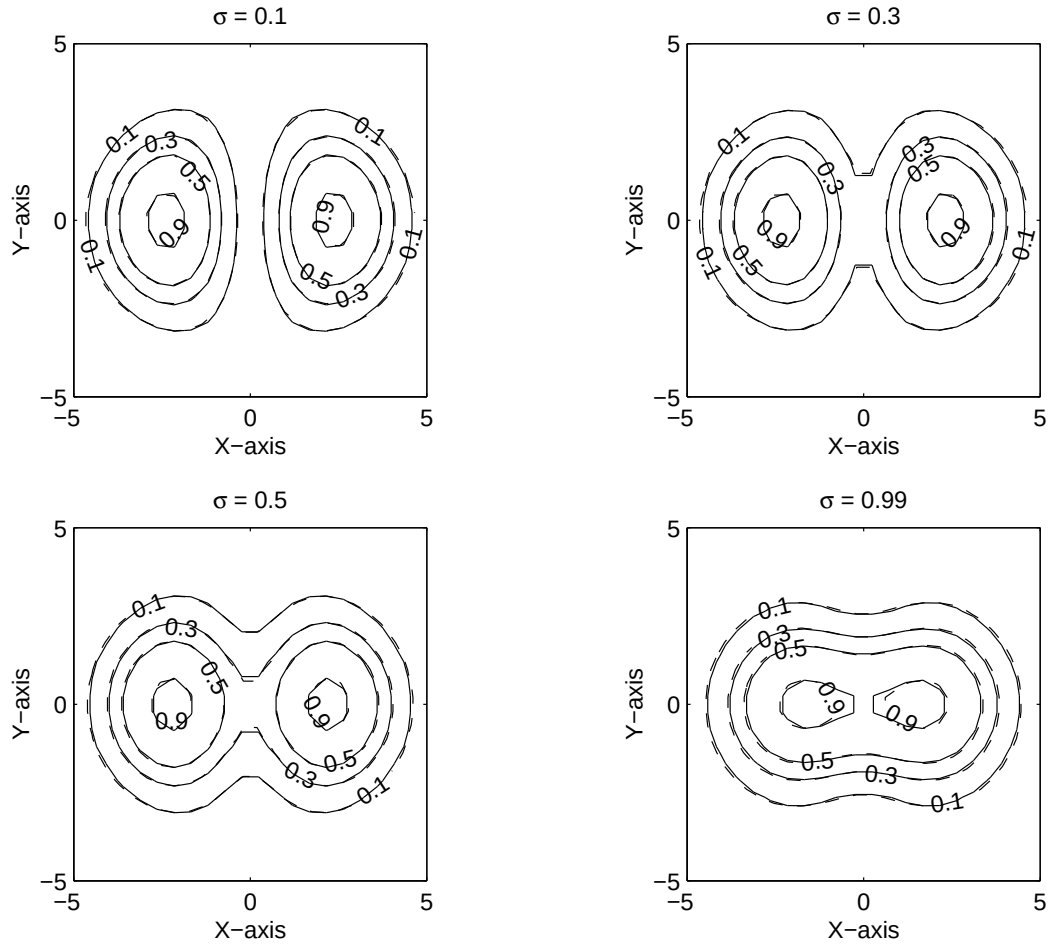

Figure 4:

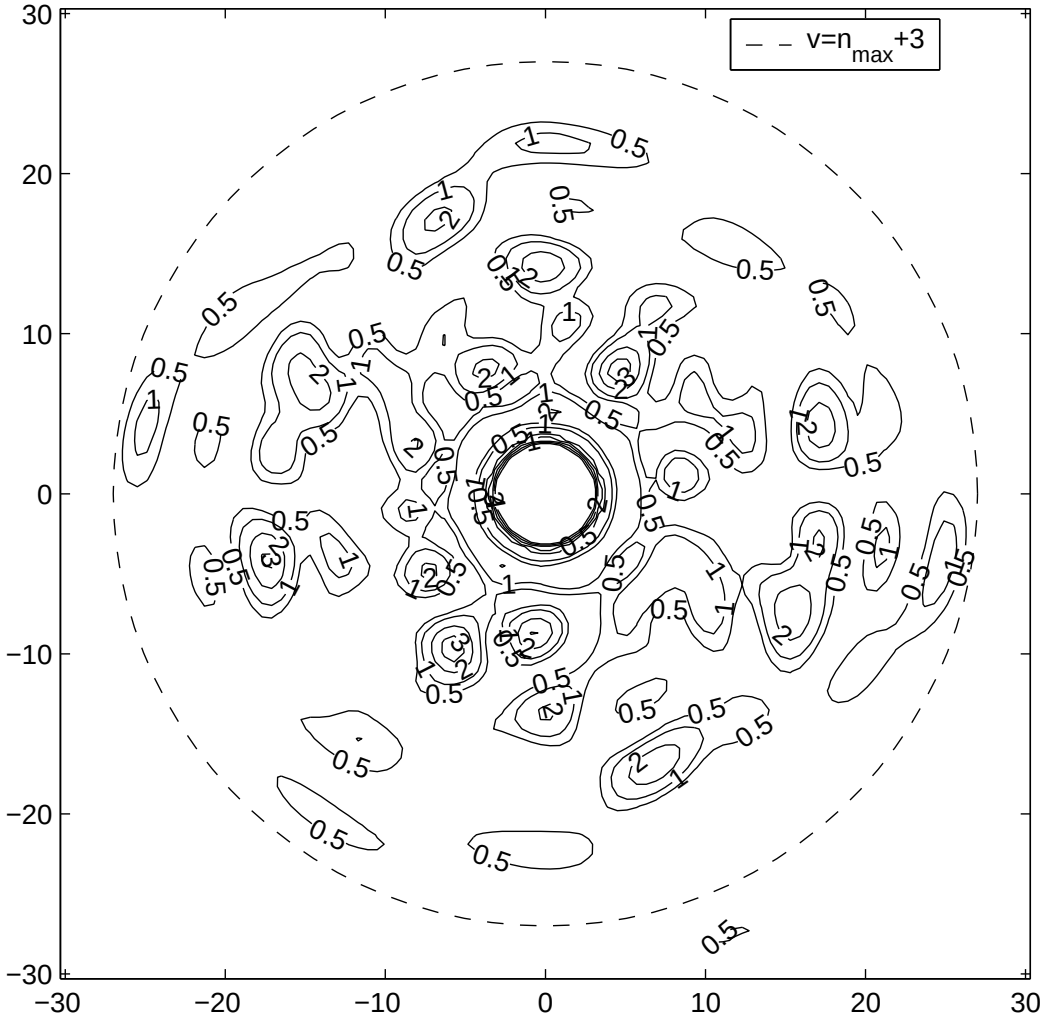

Figure 5:

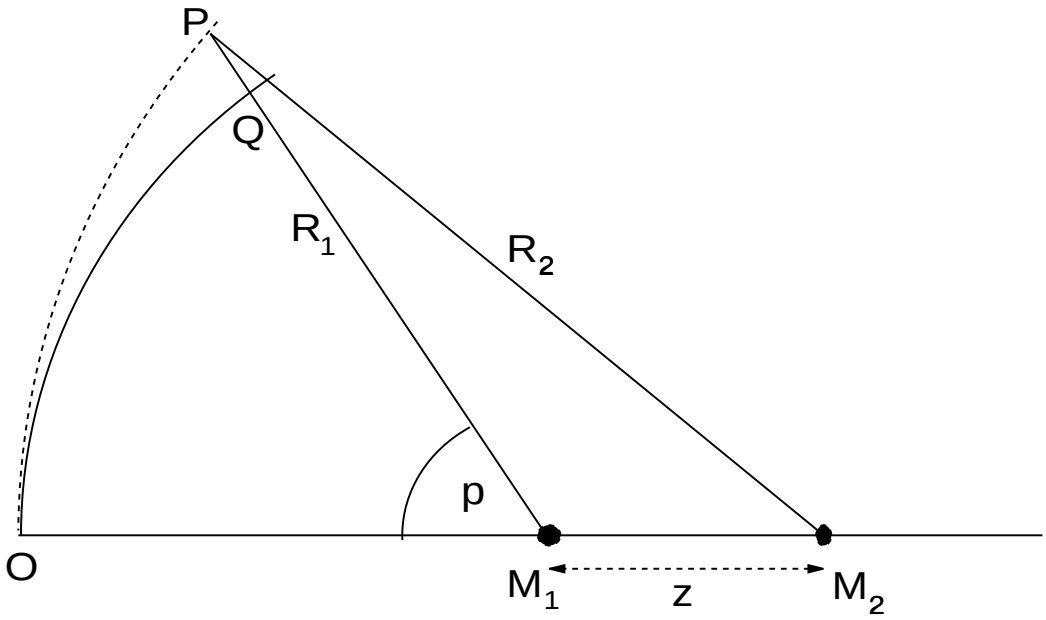

Figure 6: